Conductance of perovskite oxide thin films and interfaces

Mubeen Dildar, I.

Cover Page

The handle http://hdl.handle.net/1887/20501 holds various files of this Leiden University dissertation.

Author: Mubeen Dildar, Ishrat
Title: Conductance of perovskite oxide thin films and interfaces
Issue Date: 2013-02-06

<div style="text-align: right;">

2

</div>

Oxide films and interfaces

This chapter provides a general introduction in the physics of manganite perovskites, both for bulk materials and in thin film form. It also provides an introduction into the phenomena encountered at interfaces of complex oxides, in particular at the interface between two insulators $SrTiO_3$ and $LaAlO_3$.

2.1   Physics of manganites

The perovskite-type manganites have the general formula $RE_{1-x}AE_xMnO_3$, where RE stands for trivalent rare earth ions such as La, Pr, and Nd and A for divalent alkaline earth ions such as Sr, Ca, and Ba. Depending on the composition, they show a variety of magnetic and electronic phenomena, including ferromagnetism, antiferromagnetism, charge and orbital ordering and magnetic-field driven metal insulator transitions. The physical properties of the manganites strongly depend on their crystal structure, and they are therefore sensitive to pressure and strain. There is a general relation between the electronic parameters and the structural modification in the perovskites which is described below.

2.1.1   The crystal structure

The manganites belong to the family of perovskites. The general formula is ABO_3 where A and B are two cations of different size and O is the anion that bonds them together. In the idealized cubic unit cell of such a compound, the A atom sits at corner positions $(0,0,0)$, the B atoms sits at body centered positions $(1/2, 1/2, 1/2)$ and oxygen atoms sit at face centered positions $(1/2, 1/2, 0)$ as shown in Figure 2.1. So, the B cations are in a 6-fold coordination surrounded by an octahedron of anions and the A cation in 12-fold cubo-octahedral co-ordination.

The sizes of the ionic radii of ABO_3 determine the so-called tolerance factor t, which measures how well the B-atom fits in the AO_6 cage. Using the radii r_A, r_B

<div style="text-align: center;">

5

</div>
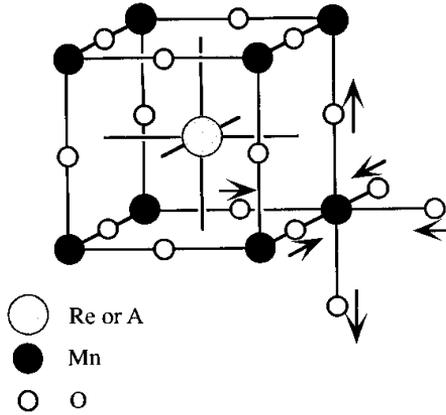
Figure 2.1: The perovskite type manganites with general formula ABO_3. Taken from ref. [10].

and r_O of the A−, B− site ions and the oxygen, t is defined as

$$t = \frac{(r_A + r_O)}{\sqrt{2}(r_B + r_O)} \qquad (2.1)$$

For cubic structures $t = 1$. In manganites, the smaller size of the A-site atoms generally leads to a smaller tolerance factor, $t < 1$. That places the B−O bonds under compression and the A−O bonds under tension. As a consequence, the oxygen octahedra have to buckle in order to fill the space around the A-site atoms. This buckling consists of rotation of the octahedra about the a, b, and c axis (a 3-axis rotation). The final effect is that the structure deforms into a Pnma orthorhombic, rhombohedral or tetragonal structure depending on the relative orientation of deformation [1].

2.1.2 Electronic features of undoped LaMnO$_3$

The undoped compound LaMnO$_3$ is a Mott insulator. Its structure has been thoroughly studied by neutron diffraction experiments [2]. Its electronic configuration allows for orbital ordering as stated below.

The Mn atom in undoped LaMnO$_3$ is surrounded by an oxygen octahedron. The configuration of the outer electrons in the manganese ion is $3d^4$. The degeneracy is lifted by the crystal field as shown in Figure 2.2. The five 3d orbitals divide into two sets of orbitals which are degenerate. The doublets are d_z^2 and $d_{x^2-y^2}$, denoted by e_g. The three lower lying triplets, d_{xy}, d_{yz} and d_{zx} are denoted by t_{2g}. The e_g orbitals are oriented towards the neighboring oxygen while the t_{2g} states
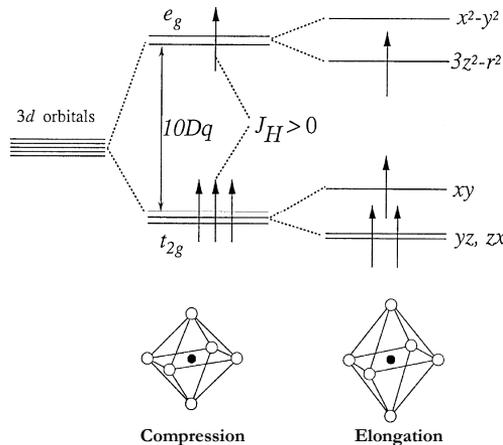
Figure 2.2: Ligand-field splitting of five-fold degenerate atomic 3d levels into lower t_{2g} (triply degenerate) and higher e_g (doubly degenerate) levels. Jahn-Teller distortion of the MnO_6 octahedron further lifts each degeneracy in compressed and elongated mode as shown in the figure, taken from ref. [13].

have nodes in these directions. This means e_g orbitals can intermix with oxygen p orbitals. The crystal field splitting between the t_{2g} and e_g is about 1 eV.

Double occupancy of an individual t_{2g} level is strongly suppressed by Hund's coupling rule and electrostatic repulsion, so the three 3d electrons in Mn^{+4} are spin aligned in the t_{2g} levels (spin S=3/2). The Mn^{+3} ion has one additional electron, which does not occupy a t_{2g} level due to strong Coulomb repulsion and the Pauli exclusion principle, but instead occupies one of the e_g levels. This electron is also strongly Hund coupled and therefore spin-aligned with the t_{2g} triplet, making S = 2.

The e_g electrons become localized when the hopping interaction is relatively small. The cause of the e_g electron localization is two-fold: one is electron correlation among t_{2g} electron and the e_g states, although e_g states are more strongly hybridized with the O 2p states. The other is the JahnTeller coupling of the e_g electron with the surrounding oxygen displacement. Such an electronic configuration has a tendency to distort its environment at the cost of elastic energy but it gains electronic energy which makes it stable. This is a consequence of the Jahn-Teller theorem which states that a cation with a ground state that is degenerate, but not a Kramers' doublet, may be stabilized by a distortion of the surroundings to some lower symmetry that removes the ground state degeneracy. This is shown schematically in Figure 2.2. The MnO_6 octahedra distort so as to give a two long and four short geometry about the MnO_6, so the z^2 orbital is occupied and the x^2-y^2 orbital empty. These z^2 orbitals can and do order in the MnO_6 planes of

7
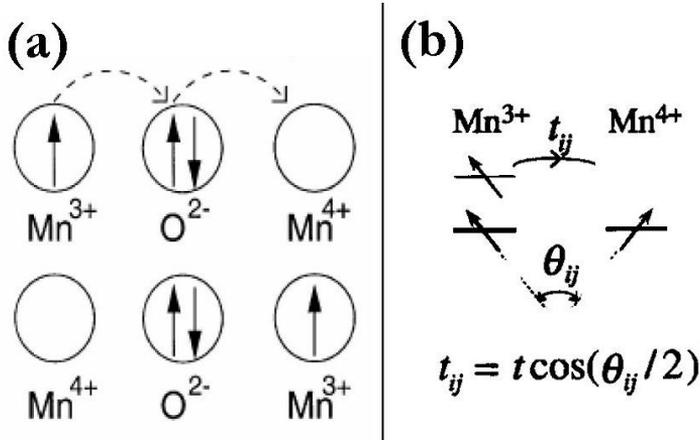
Figure 2.3: (a) A charge transfer in double exchange mechanism, (b) Transfer integral (hopping matrix), figure taken from ref. [13]

the structures so that long and short Mn-O bonds alternate in a "checkerboard" pattern. Thus, the orbital ordering in the manganites is always associated with a cooperative Jahn-Teller distortion.

2.1.3 Doped LaMnO$_3$ & double exchange mechanism

The undoped LaMnO$_3$ is an A-type antiferromagnetic (AAF) insulator, with an antiferromagnetic coupling in one (pseudocubic) direction and a ferromagnetic coupling in the planes orthogonal to this. Doping changes the magnetic order, the compound exhibits a mixed valence character, which results in a rich phase diagram.

The Mott insulator LaMnO$_3$ can be doped by divalent impurities to create electron vacancies or holes in the e$_g$ orbital states of the crystal. This hole doping makes the Mn sublattice a mixture of Mn^{+3} and Mn^{+4}. The e$_g$ electrons escape from the long-range ordering and can become itinerant. They hop between Mn^{+3} ion and Mn^{+4} ion with the help of the oxygen in between. This process is called the double exchange mechanism.

The basic idea of double exchange (DE) as a mechanism for electrical conduction in the manganites was postulated by Zener [3]. In the initial model there was the simultaneous transfer of one electron from a manganese 3d e$_g$ orbital to an oxygen 2p orbital and transfer from the same orbital to a manganese 3d e$_g$ orbital on an adjacent ion as shown in Figure 2.3. In this way the e$_g$ electrons are able to move throughout the lattice. Both electrons involved in the exchange must have the same spin (because of the Pauli exclusion principle). This leads to a ferromagnetic arrangement of the e$_g$ electrons.

Further theoretical work was performed by Anderson and Hasegawa [4] and de Gennes [5]. In the limit of large Hund coupling, the spin of the e$_g$ electron is tied

to the core t_{2g} spin and the hopping parameter t varies as

$$t_{ij} = b(\cos\frac{\theta_{ij}}{2}) \ (J_H >> T) \tag{2.2}$$

where θ_{ij} is the angle between the core t_{2g} spins on adjacent manganese ions, which depends only on the relative orientation of the two spins and not their absolute direction with respect to the crystallographic axes [4]. The kinetic energy of the e_g electron is proportional to t_{ij}. Thus, in the DE model, if the manganese spins are arranged ferromagnetically then t_{ij} will be maximized and the electrons become itinerant. Therefore, ferromagnetism and metallicity are intimately linked. The basic DE model is in qualitative agreement with the experimental data. However, Millis *et al.* have shown that a Hamiltonian incorporating only the DE interaction cannot explain the change in magnitude of resistance at the metal-insulator transition [6]. A very strong electron-phonon coupling stemming from a Jahn-Teller splitting of Mn^{+3} ion, causes a local lattice distortion of the oxygen octahedra and traps the electron in the crystal lattice called polaron, resulting in increase in resistance at MI transition. A CMR effect where the large decease in resistance under magnetic field occurs, can also be explained on basis of electron-phonon coupling. The localization of conduction band electrons as polaron can be turned off by the application of magnetic field, a significant decrease in resistance under magnetic field, as T is decreased through T_c, permitting the formation of a metallic state [7–10].

2.2 Phase diagram of $La_{1-x}B_xMnO_3$, B=Ca,Sr.

As discussed before, the static collective Jahn Teller distortion present in $LaMnO_3$ is removed with increase in the doping level, and thereby the amount of Mn^{4+}. Introducing divalent Ca^{2+} or Sr^{2+} impurities therefore leads to different phases, with different conducting and magnetic regimes. This will be briefly sketched below, following the concentration x of the dopand atom, and the phase diagram given in Figure 2.4.

x<0.2; insulating state

Increasing the doping to x= 0.1 does not change the A-type antiferromagnetic ground state qualitatively. A small net magnetic moment appears due to spin canting effects, or droplet-like phase separation. The material is insulating. Above, x= 0.1, the system becomes ferromagnetic, although still insulating. Apparently, although the e_g electron is mostly localized, it can already convey spin information to neighbor sites. The ferromagnetic transition temperatures T_c rises steeply with increasing doping, from 150 K to 250 K (Sr-doping) or 170 K (Ca-doping). In LCMO, the additional effects of charge ordering is found below 80 K. This is due to the larger Mn-O-Mn bond angles in the Ca-system.
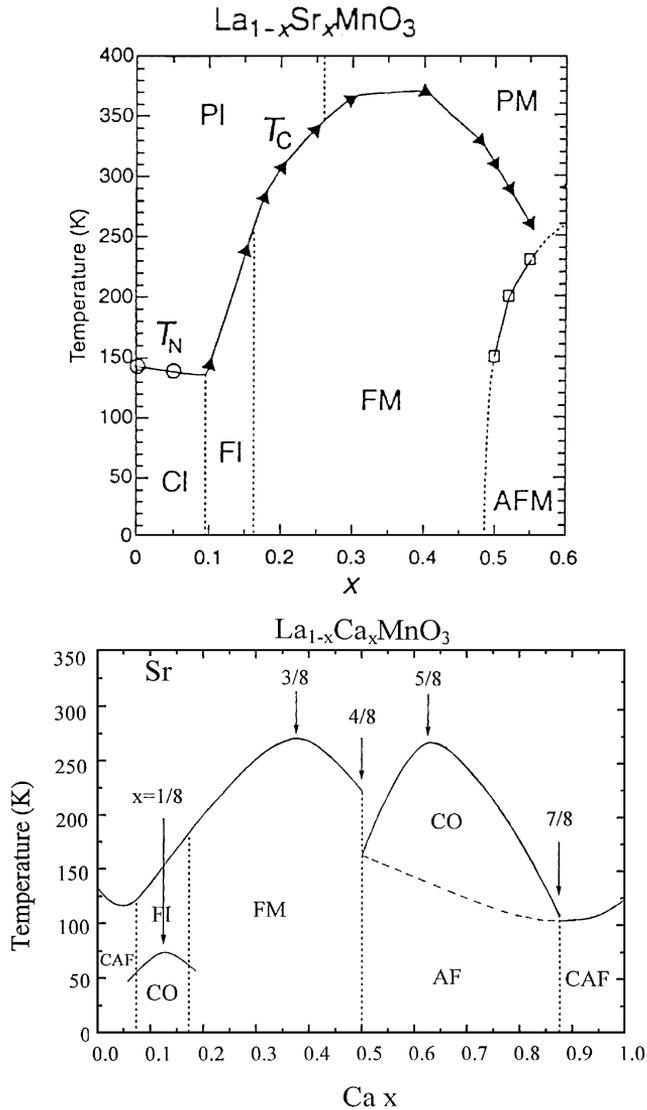
Figure 2.4: Phase diagram of (a) $La_{1-x}Sr_xMnO_3$ taken from references [11–13], (b) $La_{1-x}Ca_xMnO_3$ taken from reference [13]. They are constructed from measurements of macroscopic quantities such as the resistivity and magnetic susceptibility, reproduced from FM: Ferromagnetic Metal, FI: Ferromagnetic Insulator, AF: Antiferromagnetism, CAF: Canted AF, and CO: Charge/Orbital Ordering. FI and/or CAF could be a spatially inhomogeneous states with FM and AF coexistence.

0.2>x<0.5, the ferromagnetic metallic state

Doping beyond x = 0.2 leads to the formation of a band and a ferromagnetic metallic state (FM). T_c further increases to 350 K (LSMO) or 260 K (LCMO). The difference is again due to the difference in bond angles, leading to a larger band width for the Sr-doped system. The maximum in T_c is reached around x = 0.3 - 0.35. in the FM state, the distinction between Mn^{3+} and Mn^{4+} ions is lost, and the collective Jahn-Teller distortion have disappeared. Above T_c, where the material becomes paramagnetic and insulating, the residual conductance can be described by polaron hopping [7, 10], which means that (dynamic) lattice deformations are still present. This is the phase where Colossal Magnetoresistance occurs, because of the sensitivity of the electronic motion to the spin directions and therefore an applied magnetic field.

Lynn *et al.* used neutron scattering measurements to discover the formation of combined structural/magnetic polarons in LCMO cubic systems at the metal-insulator transition [14]. The formation of these nanoscale polarons truncates the ferromagnetic phase, and thus explains the first-order nature of the transition. These polarons form a well-defined thermodynamic glass phase above the ferro-magnetic ordering temperature, which then melts into a polaron fluid at higher temperatures. They also suggested this polaron glass as an additional phase in the refinement of the phase diagram of LCMO.

x≈0.5, Antiferromagnetic and charged ordered state

For the bulk material of LCMO, at x=0.5, two transitions are seen on cooling. A ferromagnetic state is initially entered at around 230 K. At lower temperatures, there is a transition to an antiferromagnetic state. The Neel temperature is approximately 135 K on cooling and 185 K on warming [15]. This thermal hysteresis is typical of a first-order phase transition in the presence of pinning. Additionally, phase coexistence between ferromagnetic and charge ordered phases has been seen in bulk samples of $La_{0.5}Ca_{0.5}MnO_3$ [16] and a charge-ordered ferromagnetic phase was observed at 90 K [17]. It therefore appears that the low-temperature boundary between the ferromagnetic and antiferromagnetic phases is not sharp and there is a mixed-phase region around x = 0.5.

0.5>x<1, the antiferromagnetic state

Values of x in the range 0.5<x<1 give a charge-ordered (CO) insulator as the low-temperature ground state. In a CO state, the Mn^{+3} and Mn^{+4} ions arrange themselves into two distinct sub-lattices to form a series of stripes of the two types of ions [18]. Well ordered structures are formed when the ratio between Mn^{+4} and Mn^{+3} is integer, such as 1:1,1:2 etc. For other levels of doping, the ordered structure comprises extra planes of one type of Mn ion to obtain the correct chemical composition [19]. There is an additional transition on further cooling, in which the manganese spins align themselves in an anti-parallel arrangement to form an antiferromagnet. This occurs in the range 100 - 150 K and the Neel temperature

11

T_N depends on the level of calcium doping. Neutron studies suggest that this phase is a CE type antiferromagnetic with a checkerboard arrangement of spins [2]. For LSMO, for $0.5 > x < 0.6$ an interesting A-type antiferromagnetic metallic state is stabilized.

2.3 Electronic transport in thin films of metallic manganites

$La_{1-x}Ca_xMnO_3$ and $La_{1-x}Sr_xMnO_3$ are interesting candidates to study the fundamental physics of the interplay between electronic, magnetic and lattice degree of freedom. This can lead to quite complicated phase diagrams, as shown above. Another dimension, however, is given by studying manganite thin films, which adds the effects of strain (by the substrate) and disorder to the other ingredients. Especially very thin films (20 nm and below) are of interest here. In this regime, strain can be uniform, electric fields can penetrate to a significant degree and the effects of the interface become important and can be studied. Different doping regimes can be of interest, and much work has been devoted to the regime around x = 0.2, on the border between the insulating and metallic states. Here, we concentrate on the more homogeneous regime around x = 0.35. This doping level gives the highest Curie temperatures, 370 K in bulk $La_{0.7}Sr_{0.3}MnO_3$ and 250 K in bulk $La_{0.7}Ca_{0.3}MnO_3$. In thin films these values are usually lower, as we shall see below, but the basic physics is the same. Figure 2.5 shows magnetoresistance and magnetization measurements of two films on $SrTiO_3$ (STO) substrates, of a 7 nm LSMO and a 9 nm LCMO film. The resistivity is seen to peak strongly at the onset of magnetization, which is the hallmark of the transition from the high temperature, semiconducting and polaron dominated regime to the low temperature ferromagnetic metallic regime. Note that the peak temperature T_p is close to the Curie temperature T_c, and can be taken as a measure for the latter. One of the focus point of this thesis is the possible connection between strain and the amount of carriers in the films. Below, we therefore briefly discus the known effects of strain and the basis of the Hall effect, which can be used to measure the carrier density.

2.3.1 Effect of strain in thin films of manganites

The phase diagram shown in Figure 2.4 refers to bulk single crystalline materials. The properties of manganites can change in case of epitaxial thin films and additional effects can be studied as a function of thickness [21] or strain which can be either tensile or compressive, depending on the substrate [22].

The major effects of strain derive from the double exchange mechanism and its sensitivity to bond lengths and bond angles. Moreover, deformations of the oxygen octahedra reinforce the tendency to Jahn-Teller deformations. Generally, strain therefore leads to smaller bond lengths and lower Curie temperature. Strain can be induced by the lattice mismatch between substrate and film. If the lattice
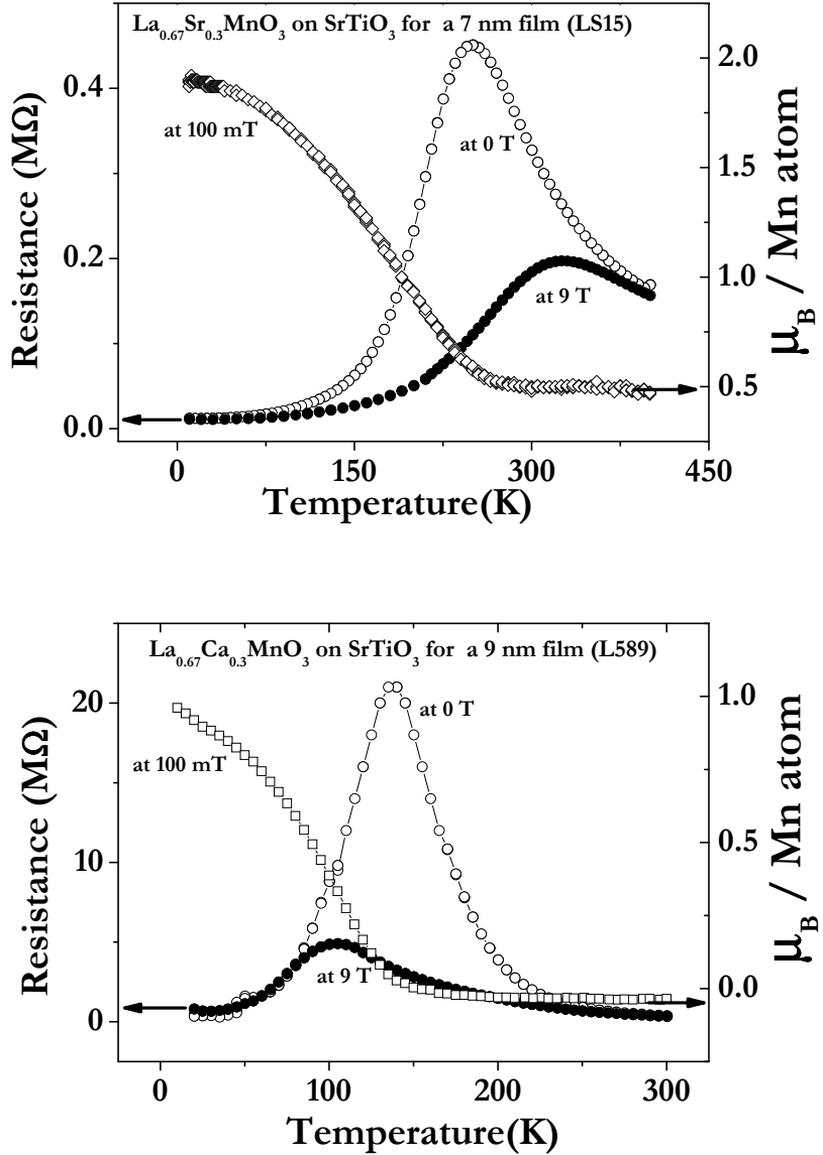
Figure 2.5: Transport and magnetic properties of thin films of (top) $La_{0.67}Sr_{0.33}MnO_3$ on $SrTiO_3$ for 7 nm, (bottom) $La_{0.67}Ca_{0.33}MnO_3$ on $SrTiO_3$ for 9 nm. Both are own data taken on sputter-grown films.

constant of the film is larger than that of the substrate, the strain is compressive. For the other way round, the strain is tensile. If the lattice constant of the film is larger than the substrate, it is compressive strain and if the lattice constant of substrate is larger than the film, it is tensile strain. The relevant parameter here is the mismatch f, given by

$$f = \frac{a^f - a^s}{a^s}\% \tag{2.3}$$

where a^f refers to the lattice constant of film, a^s for the substrate and 'f' is the mismatch.

The lattice strain has direct implication with Poisson's effect where the elastic properties of thin films propose a change between crystal axis and the bonds within the material lattice to accommodate the stress. When the bonds elongate in the direction of load/force/initial change, they shorten in the other directions. The same formalism in manganites is sensitive to both Mn-O bond distance (d_{Mn-O} and Mn-O-Mn bong angle (θ)). These parameters directly influence the case of electron hopping between Mn ions. Under the effect of strain, the slight changes in d_{Mn-O} and θ can also change the on-site coulomb correlation energy and/or bandwidth. This may lead to an metal-insulator transition/ferromagnteic ordering slightly suppressed as compared to the bulk material. Moreover, the co-operative nature of Jahn-Teller (JT) effect makes these materials much susceptible to strain.

2.3.2 On the critical thickness

Since this thesis will be much concerned with very thin films, it is relevant to mention here the issue of the critical thickness of manganite thin films, in particular LSMO and LCMO. It is generally found that bulk-like magnetic and electronic properties only develop beyond a certain (critical) thickness, resulting in a "dead layer" of a few nm. For a LSMO, early work of Sun *et al.* an electrically dead layer of about 3 nm (growth on NGO) to 5 nm (growth on LAO) was observed [23]. It was noted that, given the differences in lattice parameters, strain did not appear to be the driving factor. The issue was also discussed by Huijben *et al.*, who studied thin films of LSMO grown on STO (001) and found an electrically and magnetically dead layer of about 10 unit cells, or 4 nm [24]; and by Kim *et al.* who reported a critical thickness of 8 u.c's when growing on $(LaAlO_3)_{0.3}$ $(SrAl_{0.5}Ta_{0.3}O_3)_{0.7}$ (LSAT), where strain is minimal [25]. Similar findings were reported for LCMO by Bibes *et al.* using nuclear magnetic resonance, found a layer of about 5 nm to nonferromagnetic and insulating when grown on STO [26]. Zanderbergen *et al.* found a critical thickness of about 6 nm [27], similar to de Andres *et al.*, growing on STO and NGO [28].

While dead layers are therefore well documented, their cause is not fully clear. At least three ingredients play a role. One is the oxygen content; one may be the presence of a polar discontinuity, which will be discussed later; one is the difference in structure which may occur in very thin films due to the lattice mismatch. It was shown by Yang *et al.* for instance, that the microstructure of very thin films of LCMO on STO is different from the bulk: the structure is 2-tilt rather than
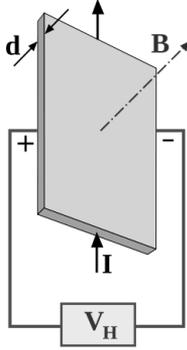
Figure 2.6: A schematic diagram to measure Hall voltage.

3-tilt [29]. Very recently, in a similar vein, it was shown that octahedra rotation in very thin films of LSMO on STO leads to special magnetic configuration around a thickness of 9 u.c or 3.5 nm [30].

2.3.3 Hall effect in manganites

The Hall effect is the voltage which appears as a result of current applied in a conductor under the influence of an applied magnetic field [31].

Figure 2.6 shows the experimental geometry to produce this effect. The setup is usually arranged such that the magnetic field, current and resulting Hall field are all perpendicular to each other. When an electric current flows through a conductor in a magnetic field, the field exerts a transverse force (Lorentz force) on the moving charge carriers which pushes them to one side of the conductor. A buildup of charge at the sides of the conductors will balance this magnetic influence, producing a measurable voltage between the two sides of the conductor, the Hall voltage. For a simple metal with a spherical Fermi surface and only one type of charge carrier (electrons) the Hall voltage V_H across a thin metallic plate is given by

$$V_H = -\frac{IB_z}{ned} \tag{2.4}$$

where I is the current across the plate length, B_z is the magnetic field perpendicular to the plate, d is the thickness of the plate, e is the elementary charge, and n is the charge carrier density. Denoting the current density by j_x, and the Hall electric field E_y, the quantity known as the Hall coefficient is then defined as

$$R_H = \frac{E_y}{j_x B_z} \tag{2.5}$$

By setting the force from the electric field equal to the Lorentz force, the Hall coefficient in the free electron approximation is given by

$$R_H = -\frac{1}{ne} \tag{2.6}$$

a) Intrinsic deflection

Interband coherence induced by an external electric field gives rise to a velocity contribution perpendicular to the field direction. These currents do not sum to zero in ferromagnets.

E

$$\frac{d\langle \vec{r}\rangle}{dt} = \frac{\partial E}{\hbar \partial \vec{k}} \left(+ \frac{e}{\hbar} E \times b_n \right)$$

Electrons have an anomalous velocity perpendicular to the electric field related to their Berry's phase curvature

b) Side jump

The electron velocity is deflected in opposite directions by the opposite electric fields experienced upon approaching and leaving an impurity. The time-integrated velocity deflection is the side jump.

c) Skew scattering

Asymmetric scattering due to the effective spin-orbit coupling of the electron or the impurity.

Figure 2.7: Three mechanisms of anomalous Hall effect. The figure is taken from reference [46].

This is used to determine the sign and number of charge carrier when only one type is involved, the one-band model. In semiconducting materials, both electrons and holes play a role, and since they reside in different bands, with different masses and mobilities, R_H is given by

$$R_H = \frac{n_h \mu_h^2 - n_e \mu_e^2}{e(n_h \mu_h + n_e \mu_e)^2} \tag{2.7}$$

where n_h is the carrier density of holes, n_e is the carrier density of electrons, μ_h is the mobility of holes and μ_e is the mobility of electrons.

Hall effect in ferromagnetic Materials

In ferromagnetic materials, there is an an additional contribution to the Hall voltage caused by scattering of electrons from magnetic moments [32]. This extra term is proportional to the magnetization M of the sample [33]. This can be written as

$$\rho_H = \mu_0 (R_H H_a + R_A M) \tag{2.8}$$

where now H_a is the applied magnetic field, R_H is the ordinary Hall co-efficient and R_A is the coefficient describing the so-called anomalous Hall effect (AHE).

The origin of the AHE is not trivial, and different ideas have been developed to explain this phenomenon. The first theoretical explanation of the AHE was given by Karplus and Luttinger and the AHE was considered to originate from spin-orbit interactions causing population imbalance of electronic spin states and asymmetric motion of electrons. The effect is intrinsic [35]. Smit *et al.* found that above treatment of the AHE is beyond the usual Bolztmman transport theory. He stated that impurity scattering is essential for the steady state and hence also for AHE [37]. That mechanism was named skew scattering. Skew scattering describes the average deflection of the trajectory of a charge carrier in a scattering event, and yields a contribution which is proportional to the Bloch state transport lifetime. It dominates more in nearly perfect crystals. After that Luttinger developed the systematic theory for AHE in the presence of the impurity scattering [36]. The third mechanism of the impurity-induced AHE, is the side jump model which was proposed by Berger [38, 39]. He proposed that the center of mass of a wave packet undergoes a discontinuous and finite sideways displacement on scattering by a center potential, in the presence of spin orbit interaction. The asymmetric scattering of spin polarized electrons make skew scattering and side jump mechanisms as extrinsic AHE.

The two extrinsic terms can be related to the longitudinal resistivity as

$$\rho_{AH} = a\rho_{xx} + b\rho_{xx}^2 \qquad (2.9)$$

The linear term on the right is called "skew scattering" and the quadratic is "side jumps" respectively. They both differ and depend by amount of disorder in the sample. The anomalous contributions to the Hall effect are shown in Figure 2.7. For a complete theoretical background, some reviews are given in Ref. [45, 46].

2.4 Interfaces of complex oxides

Next to the electronic properties of very thin manganite layers, a significant part of this thesis is on the subject of the properties of an interface between the complex oxides. In particular, the issue of the formation of a two-dimensional electron gas (2DEG) at LAO/STO is investigated. The physics behind the formation of a two dimensional electron gas at the interface of the band insulators $LaAlO_3$ and $SrTiO_3$ is still subject to an ongoing debate even eight years after its discovery [47]. The basic idea is that polar $LaAlO_3$ on non-polar $SrTiO_3$, singly terminated by TiO_2, generates a high mobility quasi two-dimensional electron gas at the interface due to an electronic transfer mechanism (electronic reconstruction). The interface becomes conducting only when the $LaAlO_3$ thickness reaches a critical value of 1.6 nm (4 unit cells of $LaAlO_3$) and $SrTiO_3$ is singly terminated by TiO_2 [48, 49]. These observations have mostly been made on samples grown by Pulsed Laser Deposition (PLD).

In this section, we give a brief summary of existing work on LAO/STO interfaces. We review the basic properties and discuss the mechanisms which have been claimed to be responsible for the observed conductance at the interface.
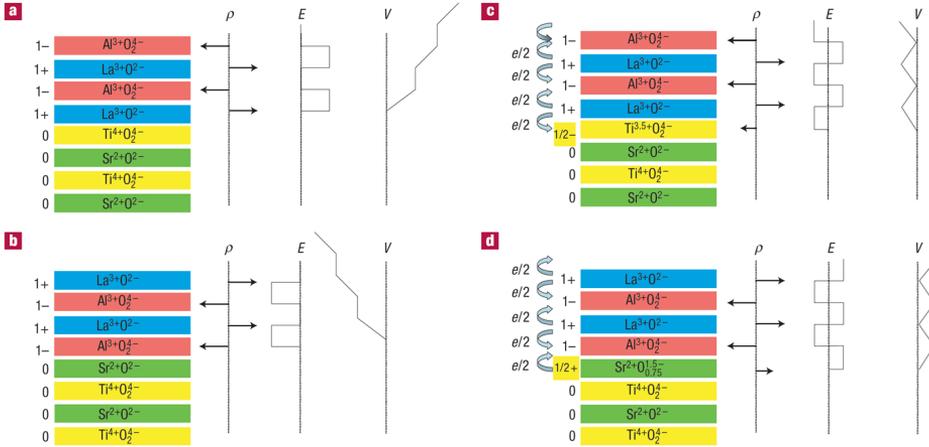
Figure 2.8: An intrinsic electronic reconstruction to avoid polar catastrophe for LAO/STO interfaces, adapted form Ref. [58]

2.4.1 Intrinsic Electronic reconstruction

The pioneering work to make conducting interfaces of LaAlO$_3$ and SrTiO$_3$ was that of Ohtomo and Hwang using pulsed laser deposition [47]. Both constituents are conventional band insulators but they differ in layer-to-layer charge variation. The interface therefore shows a charge discontinuity, the so-called polar discontinuity or catastrophe.

The intrinsic electronic reconstruction which arises from the polar catastrophe can be understood with the help of figure 2.8 where alternating layers of polar LAO (LaO$^+$, AlO$_2^-$) and non-polar STO (SrO, TiO$_2$) are stacked. The charged layers can be considered as parallel plates of capacitors. The potential across each capacitor (each layer of LAO) is additive and should increase with increasing number of plates (LAO layers). To avoid a diverging potential, half an electron should be compensated at the interface. This doping allows the reconstructed interfaces to be n-type (charge carriers; electrons) or p-type (charge carriers; holes). However, only the n-type interface is found to be conducting while p-type is insulating. The valence change of Ti from Ti^{+4} to Ti^{+3} allows the construction of n-type interface.

Critical thickness for LaAlO$_3$ films

The same study raised another interesting observation on the minimum thickness of the LaAlO$_3$ film before mobile carriers and conductivity are observed at the n-type interface. This critical thickness is 4 unit cells on samples grown in a background oxygen pressure of 1.3×10^{-4} mbar [47]. The interface is insulating below this thickness. Thiel *et al.* [48] showed that after annealing, the sheet carrier density n$_s$ for samples grown at the same pressure with fewer than 4 unit cells of LaAlO$_3$
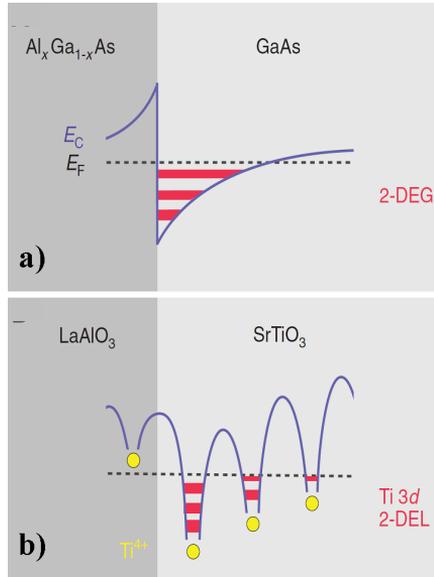
Figure 2.9: (a and b) Comparison between two-dimensional electron systems generated at interfaces between standard semiconductors, for example, between GaAs and $Al_xGa_{1x}As$ (a) and between $LaAlO_3$ and $SrTiO_3$ (b) taken from Ref. [53].

is below detectable levels. Above 4 unit cells, they observe a step-like jump in n_s but the value of the sheet carrier density is smaller than the theoretical value of 0.5 e/a_{STO}^2 or $3.3 \times 10^{14} cm^{-2}$. The small sheet carrier densities suggest that not all electron are participating in the transport. Huijben *et al.* [51] grew np-type interface samples with pressure of oxygen 10^{-5} mbar without annealing and observed that the samples are conducting for all $LaAlO_3$ thickness studied.

The sheet carrier density starts out small but finite for 1 u.c of $LaAlO_3$ and it increases with $LaAlO_3$ thickness until it saturates at $1.4 \times 10^{14} cm^{-2}$ for ≥ 6 u.c of $LaAlO_3$. A theoretical study [52] on this issue favors the polar-nonpolar mechanism to be already valid for a one unit cell $LaAlO_3$ film, but in growing $LaAlO_3$ on $SrTiO_3$ may need some sacrificial layers to compensate surface defects and before the interface becomes conductive at 4 unit cells of $LaAlO_3$.

Band offset and band-bending

As intrinsic electronic reconstruction on oxide interfaces would be followed by band bending and band offset like semi-conducting interfaces. Scanning tunnelling spectroscopy measurements of the density of states at the $LaAlO_3$-$SrTiO_3$ interface [53] revealed remarkable differences between this two-dimensional electron system and the 2DEGs formed at interfaces between conventional semiconductors. As sketched in Figure 2.9a, at the semiconductor interface the mobile electrons move in two-dimensional subbands within the quantum well generated by band bending. At
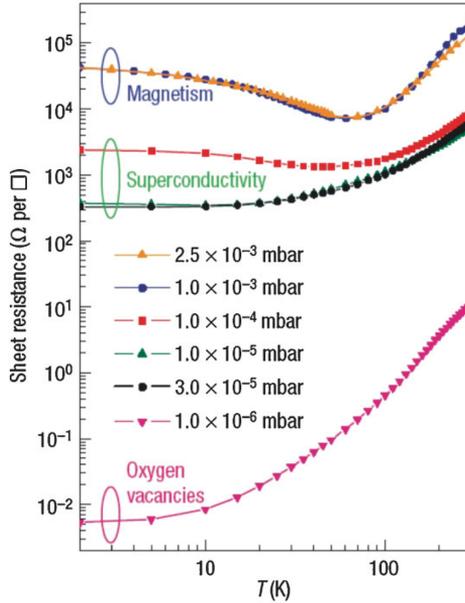
Figure 2.10: Conductivity of LAO/STO interface changing with background oxygen pressure and temperature, taken from Ref. [57]

the oxide interface, however, there are multiple quantum wells given by the ionic potentials of the TiO_6 octahedra, and within each quantum well are subbands that are a subset of the Ti 3d states (Figure 2.9b). In these bands, the electrons are subject to the correlations of the Ti 3d orbitals and form a two dimensional electron liquid rather than an electron gas.

2.4.2 Oxygen Vacancies

$SrTiO_3$ as a substrate is very sensitive to disturbances such as annealing or argon ion bombardment. In particular, the role of oxygen vacancies at the interface of LAO/STO is crucial. Pulsed laser deposition is a low pressure technique where the intensity of the plasma changes with the background pressure. In the case of conducting interfaces of $LaAlO_3$ and $SrTiO_3$, this background oxygen pressure has significant effects on the conductivity [54]. A low growth pressure results in high conductivity and vice versa. Ohtomo & Hwang [47] discussed the possibility of oxygen vacancies forming at low pressures (10^{-6} mbar) but excluded them above 10^{-4} mbar. They argued that the substrate remains non-conducting while subjected to the growth conditions without growing films, and if oxygen vacancies would be the origin then p-type interface should also be conducting. The reasoning is not enough to exclude the possibilities of oxygen vacancies since their role may be the facilitator rather than the generator.

The properties of interfaces can be related to four different regions of oxygen pressure; (i) a three dimensional bulk conductivity is observed at an oxygen pressure of 10^{-6} mbar. It is agreed that this pressure produces oxygen defects in $SrTiO_3$ which in turn enhance the conductivity [47], (ii) two dimensional conductivity around $pO_2 = 10^{-4}$ mbar where superconductivity effects [61] are observed at 200 mK, (iii) still a two dimensional conductivity but magnetic effects [57] are observed at 10^{-3} mbar and (iv) a badly conducting interface at high oxygen pressure, 10^{-2} mbar [55, 56]. This suggests that the background oxygen pressure plays a key role in the conductances of the interface and the above trend shows that even higher pressure should further decrease the conductance. Figure 2.10 gives an overview of resistance versus temperature behavior in the different regimes.

The reduction of STO was thoroughly studied by Scullin *et al* [65]. It was shown that annealing (450°C, 10^{-7} torr, 10 - 60 minutes) reduces an STO (001) substrate roughly over 5 nm into the crystal, but that the same crystals are reduced throughout their 500 μm thickness when coupled with PLD. So, a question is whether the most often used PLD growth parameters of LAO films on STO (750°C - 850°C, 10^{-5} - 10^{-3} torr) would be enough to reduce STO substantially beyond the interface (thickness 1 nm), and so facilitate the conduction at the interface.

2.4.3 Intermixing Effects

The idea of an abrupt interface came to an end when Nakagawa *et al.* [58] found that the n-type interface is significantly rougher than p-type interface, using atomic-resolution electron energy loss spectroscopy (EELS). They suggested that the electronic dipole energy connected with the finite width of the electron gas can be reduced by exchanging Sr with La across the interface. Willmott [59] analyzed the interface structure using Coherent Bragg rod (COBRA) analysis combined with DFT calculations and concluded that the interface is not abrupt but shows a graded intermixing over 3 unit cells. Sr and La intermix at a greater depth ($\sim$ 6 Å further away from interface) than Ti and Al ions because of larger radii and form two monolayers of $La_{1-x}Sr_xTiO_3$. This intermixing is largely accepted to exist. Recently, Chambers [52] measured the intermixing effects at the interface by Rutherford backscattering, time of flight secondary ion mass spectrometry and electron energy loss spectroscopy. He found that including intermixing effects is essential to correctly model the outcomes of these techniques to account for the electric properties of interfaces. The question still remains what procedures could reduce such intermixing to create ideal interfaces.

2.4.4 Conducting interfaces made by MBE and cationic stoichiometry

All mechanisms discussed in the previous paragraphs have been studied on interfaces made by PLD. Interfaces grown by molecular beam epitaxy raised the issue of cation stoichiometry. This issue is not touched upon in PLD-grown interfaces till date.
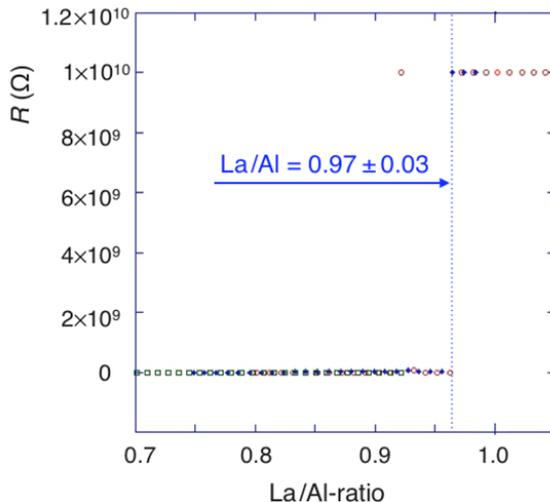
Figure 2.11: The ratio of La and Al versus resistance of the interface. Taken from Ref. [60].

In an MBE chamber, $La_{1+x}Al_{1-x}O_3$ films were grown by depositing La and Al from oppositely positioned effusion cells. Conductivity, film composition by RBS and interface structure and composition by HRTEM/EELS was measured as x was systematically changed between 0.1 and -0.1. It was found that conductivity occurs only in Al-rich films for which the La/Al atom ratio is 0.97 or less. Moreover, all HRTEM/EELS specimens showed some La diffused into the STO although not all were conducting.

For the RBS analysis, in order to move the Al RBS peak away from the substrate backscattering, STO films were grown on MgO (111) substrates and then the LAO film was grown on STO thin films. This procedure allowed the Al concentration to be measured with higher accuracy than when LAO is grown directly on bulk STO (001). This investigation strongly suggests that defects associated with non stoichiometry in the Al-rich direction may be required to activate conductivity.

2.4.5 Oxide interfaces versus semiconductors and devices

The physical phenomena which plays a role at oxide interfaces have more dimensions than conventional semiconductor interfaces. First the nature of interactions is different between the constituent electrons in interfaces of oxides and semiconductors. The electronic states of semiconductors are well described by single particle band theory. In complex oxides, however, there are strong correlations between the tightly bound transition metal d electrons and d-electrons can no longer independent but influence the behavior of all other electrons in the crystal. At interfaces in strongly correlated systems, the correlation parameters may be changed to values that are unachievable in the bulk. This complex character of the participant

materials makes it difficult to an intrinsic polar-nonpolar nature for the 2DEG as in semiconductors .

The key factors controlling the electronic behavior at oxide interfaces are ionicity, oxygen, electronic correlations and reconstruction [66]. Due to strong ionic character of oxides, the electronic orbitals tend to overlap less than the hybridized s-and p-orbitals which are characteristic of standard semiconductors. The characteristic bandwidth of oxides is less and effective masses exceed those of semiconductors, which enable the carriers to become localized. O^{2-} ions are quite polarizable, typically causing a large, nonlinear, and nonuniform polarizability of the lattice. Because the carrier density at oxide interfaces is high (10^{13} to 10^{14}/cm^2, as opposed to the 10^{11} to 10^{12}/cm^2 found in semiconductor heterostructures), this polarizability often leads to electrostatic screening lengths in complex oxides of 1 to 10 nm, which are smaller than typical screening lengths in semiconductors. This gives rise to more local and more confined novel interfacial properties which holds promise for smaller densities. Oxygen is also special because holes in the oxygen 2 p band may give rise to magnetism.

The two dimensional electron to be gas at oxides interfaces attract more interest due to its superconductivity behavior at 200 mK [61] and magnetism [57]. The flow of electrons can be controlled by an external electric field [48,62] analogous to conventional transistors. The possibility to 'write' and 'erase' conducting wires at the interface between LAO and STO with the tip of an atomic force microscope (AFM) [67], taking the first step towards highly dense nanodevices. The combination of all these properties in interfaces of oxides (totally different from the bulk) not only developed interest to understand its fundamental physics but also helped to improve technological applications. A variety of two dimensional electron systems can be stabilized at the oxide interfaces, exploiting spin, charge and orbital interaction as well as lattice vibrations. It was immediately realized that it can be the next generation of silicon based devices although achieving the mobility levels and purity seen in semiconductor heterostructures still remains a challenge. The confined electrons at the interface can be used to excite multiple electron and thus a step towards new type of solar cells [68].

Bibliography

[1] J.B. Goodenough and J.M. Longo, Magnetic and Other Properties of Oxides and Related Compounds, Landolt-Bornstein, Vol. **4**(Springer-Verlag, New York, 1970).

[2] E.O. Wollan and W.C. Koehler, Phys. Rev. **100**, 545 (1955).

[3] C. Zener, Phys. Rev. **82**, 403 (1951).

[4] P.W. Anderson and H. Hasegawa, Phys. Rev. **100**, 675-81 (1955).

[5] P.-G. de Gennes, Phys. Rev. **118**, 141-54 (1960).

[6] A.J. Millis, P.B. Littlewood and B.I. Shraiman, Phys. Rev. Lett. **74**, 5144 (1995).

[7] A.J. Millis, B.I. Shraiman, R. Mueller, Phys. Rev. Lett. **77**, 175 (1996).

[8] H. Roder, J. Zang, and A.R. Bishop, Phys. Rev. Lett. **76**, 1356 (1996).

[9] J.-S. Zhou, J.B. Goodenough, Phys. Rev. Lett. **80**, 2665 (1998).

[10] A.J. Millis, Nature **392**, 147 (1998).

[11] A. Urushibara, Y. Moritomo, T. Arima, A. Asamitsu, G. Kido, Y. Tokura, Phys. Rev. B **51**, 14 103 (1995).

[12] H. Fujishiro, J. Phys. Soc. Japan. **67**, 1799 (1998).

[13] Y. Tokura, Colossal Magnetoresistive Oxides, Vol. **2**, Gordon & Breach Science publishers, 2000.

[14] J.W. Lynn, D.N. Argyriou, Y. Ren, Y. Chen, Y.M. Mukovskii, and D.A. Shulyatev, Phys. Rev. B **76**, 014437 (2007).

[15] J. Dho, I. Kim, S. Lee, K.H. Kim, H.J. Lee, J.H. Jung and T.W. Noh, Phys. Rev. B **59**, 492 (1999).

[16] P. Levy, F. Parisi, G. Polla, D. Vega, G. Leyva, H. Lanza, R.S. Freitas and L. Ghivelder, Phys. Rev. B **62**, 6437 (2000).

[17] J.C. Loudon, N.D. Mathur and P.A. Midgley, Nature **420**, 797 (2002).

[18] C.H. Chen, S.-W. Cheong and H.Y. Hwang, J. Appl. Phys. **81**, 4326 (1999).

[19] S. Mori, C.H. Chen and S.-W. Cheong, Nature **392**, 473 (1998).

[20] Y. Moritomo, T. Akimoto, A. Nakamura, K. Ohoyama, M. Ohashi, Phys. Rev. B **58**, 5544 (1998).

[21] M. Bibes, S. Valencia, Ll. Balcells, B. Martínez, J. Fontcuberta, M. Wojcik, S. Nadolski,and E. Jedryka, Phys. Rev. B **66**, 134416 (2002).

[22] P. Dey, T.K. Nath, A. Taraphder, Appl. Phys. Lett. **91**, 012511 (2007).

[23] J.Z. Sun, D.W. Abraham, R.A. Rao, and C. Eom, Appl. Phys. Lett. **74**, 3017 (1999).

[24] M. Huijben, L.W. Martin, Y.-H. Chu, M.B. Holcomb, P. Yu, G. Rijnders, D.H.A. Blank, and R. Ramesh, Phys. Rev. B **78**, 094413 (2008).

[25] B. Kim, D. Kwon, T. Yajima, C. Bell, Y. Hikita, B.G. Kim, and H.Y. Hwang, Appl. Phys. Lett. **99**, 092513 (2011).

[26] M. Bibes, Ll. Balcells, S. Valencia, J. Fontcuberta, M. Wojcik, E. Jedryka, and S. Nadolski, Phys. Rev. Lett. **87**, 067210 (2001).

[27] H.W. Zandbergen, S. Fresien, T. Nojima, and J. Aarts, Phys. Rev. B **60**, 10259 (1999).

[28] A. de Andrés, J. Rubio, G. Castro, S. Taboada1, J.L. Martínez, and J.M. Colino, Appl. Phys. Lett. **83**, 713 (2003).

[29] Z.Q. Yang, R. Hendrikx, J. Aarts, Y. Qin, and H.W. Zandbergen, Phys. Rev.B **67**, 024408 (2003).

[30] H. Boschker, J. Kautz, E.P. Houwman, W. Siemons, D.H.A. Blank, M. Huijben, G. Koster, A. Vailionis, and G. Rijnders, Phys. Rev. Lett. **109**, 157207 (2012).

[31] E.H. Hall, Philos. Mag. **10**, 301 (1880).

[32] E.H. Hall, Philos. Mag. **12**, 157 (1881).

[33] A.W. Smith, R.W. Sears, Phys. Rev. **34**, 1466 (1929).

[34] N. Nagaosa, J. Sinova, S. Onoda, A.H. MacDonald, N.P. Ong, Rev. Mod. Phys. **82**, 1539 (2010).

[35] R. Karpus, J.M. Luttinger, Phys. Rev. **95**, 1154 (1954).

[36] J. M Luttinger, Phys. Rev. **112**, 739 (1958).

[37] J. Smit, Physica **24**, 39 (1958).

[38] L. Berger, Phys. Rev. B **2**, 4559 (1970).

[39] L. Berger, Phys. Rev. B **5**, 1862 (1972).

[40] G. Sundaram and Q. Niu, Phys. Rev. B **59**, 14915 (1999).

[41] A. Langenfeld and P.Wölfe, Phys. Rev. Lett. **67**, 739 (1991).

[42] K.A. Muttalib and P.Wölfe, Phys. Rev. B **76**, 214415 (2007).

[43] V.K. Dugaev, A. Crépieux, and P. Bruno, Phys. Rev. B **64**, 104411 (2001).

[44] H. Meier, M.Y. Kharitonov, and K.B. Efetov, Phys. Rev. B **80**, 045122 (2009).

[45] N. Nagaosa, J. Phys. Soc. Jpn. **75**, 042001 (2006).

[46] N. Nagaosa, J. Sinova, S. Onoda, A.H. MacDonald, N.P. Ong, Rev. Mod. Phys. **82**, 1539 (2010).

[47] O. Ohtomo, H.Y. Hwang, Nature **427**, 423 (2004).

[48] S. Thiel, G. Hammert, A. Schmehl, C.W. Schneider, J. Mannhart, Science **313**, 1942 (2006).

[49] C. Bell, S. Harashima, Y. Hikita, and H.Y. Hwang, Appl. Phys. Lett. **94**, 222111 (2009).

[50] M. Huijben, A. Brinkman, G. Koster, G. Rijnders, H. Hilgenkamp and D.H.A. Blank, Adv. Mat. **21**, 1665 (2009).

[51] M. Huijben, G. Rijnders, D.H.A. Blank, S. Bals, S. van Aert, J. Verbeeck, G. Tendeloo, A. Brinkman, and H. Hilgenkamp, Nature **5**, 556 (2006).

[52] S.A. Chambers, M.H. Engelhard, V. Shutthanandan, Z. Zhu, T.C. Droubay, L. Qiao, P.V. Sushkob, T. Feng, H.D. Lee, T. Gustafsson, E. Garfunkel, A.B. Shah, J.-M. Zuo, Q.M. Ramasse, Surf. Sci. Rep. **65**, 317 (2010).

[53] M. Breitschaft, V. Tinkl, N. Pavlenko, S. Paetel, C. Richter, J.R. Kirtley, Y.C. Liao, G. Hammerl, V. Eyert, T. Kopp, and J. Mannhart, Phys. Rev. B **81**, 153414 (2010).

[54] A. Kalabukhov, R. Gunnarsson, J. Borjessen, E. Olsson, T. Claeson, D. Winkler, Phys. Rev. B **75**, 121404(R) (2007).

[55] A. Kalabukhov, Y.A. Boikov, I.T. Serenkov, V.I. Sakharov, J. Borjesson, N. Ljustine, E. Olsson, D. Winkler and T. Claeson, Euro. Phys. Lett. **93**, 37001 (2011).

[56] C. Cancellieri, N. Reyren, S. Gariglio, A.D. Caviglia, and J.-M. Triscone, Euro. Phys. Lett. **91**, 17004 (2010).

[57] A. Brinkman, M. Huijben, M. van Zalk, J. Huijben, U. Zeitler, J.C. Maan, W.G. van der Wiel, G. Rijnders, D.H.A. Blank, and H. Hilgenkamp, Nature Mater. **6**, 493 (2007).

[58] N. Nakagawa, H.Y. Hwang and D.A. Muller, Nature Mater. **5**, 204 (2006).

[59] P.R. Willmott, S.A. Pauli, R. Herger, C.M. Schleputz, D. Martoccia, B.D. Patterson, B. Delley, R. Clarke, D. Kumah, C. Cionca and Y. Yacoby. Phys. Rev. Lett. **99**, 155502 (2007).

[60] M.P. Warusawithana, A.A. Pawlicki, T. Heeg, D.G. Schlom, C. Richter, S. Paetel, J. MANNHART, M. Zheng, B. Mulcahy, J.N. Eckstein, W. Zander, and J. Schubert, Bulletin of the APS **55**, nr. 2 (2010), abstract ID BAPS.2010.MAR.B37.1.

[61] N. Reyren, S. Thiel, A.D. Caviglia, L.F. Kourkoutis, G. Hammerl, C. Richter, C.W. Schneider, T.H-. Kopp, A.-S. Ruetschi, D. Jaccard, M. Gabay, D.A. Muller, J.-M Triscone, J. Mannhart, Science **317**, 1196 (2007).

[62] A.D. Caviglia, S. Gariglio, N. Reyren, D. Jaccard, T. Schneider, M. Gabay, S. Thiel, G. Hammerl, J. Mannhart, and J.-M. Triscone, Nature **456**, 624 (2008).

[63] G. Herranz, M. Basletic, M. Bibes, C. Carretero, E. Tafra, E. Jacquet, K. Bouzehouane, C. Deranlot, A. Hamzic, J.- M. Broto, A. Bathelemy, and A.Fert, Phys. Rev. Lett. **98**, 216803 (2007).

[64] W. Siemons, G. Koster, H. Yamamoto, W.A. Harrison, G. Lucovsky, T.H. Geballe, D.H.A. Blank and M.R. Beasley, Phys. Rev. Lett. **98**, 196802 (2007).

[65] M.L. Scullin, J. Ravichandran. C. Yu, M. Huijben, J. Seidel, A. Majumdar, R. Ramesh, Acta Materialia **58**, 457 (2010).

[66] J. Mannhart, D.G. Schlom, Science **327**, 1607 (2010).

[67] C. Cen, S. Thiel, C.W. Schneider, K.E. Andersen, C.S. Hellberg, J. Mannhart, J. Levy, Nature Mat. **7**, 298 (2008).

[68] J. Heber, Enter the oxides, Nature **459**, 28 (2009).